

Radio Science®

RESEARCH ARTICLE

10.1029/2022RS007553

Special Section:

Microwave and Millimeter Wave Propagation: Modeling and Applications

Key Points:

- Using Numerical Weather Prediction software to simulate meteorological data and radio wave degradation on GSO and non-GSO Earth-Space links
- Using synthetic rain rate and MultiEXCELL model to increase the spatial resolution of rain rate from NWP software
- Rain motion detection by optical flow algorithms to increase the time resolution of rain attenuation time series

Correspondence to:

M. Razavian,
sayed.razavian@uclouvain.be

Citation:

Razavian, M., Oestges, C., & Vanhoenacker-Janvier, D. (2023). Synthetic rain models and optical flow algorithms for improving the resolution of rain attenuation time series simulated from Numerical Weather Prediction. *Radio Science*, 58, e2022RS007553. <https://doi.org/10.1029/2022RS007553>

Received 30 JUN 2022
Accepted 17 NOV 2022

Author Contributions:

Supervision: Claude Oestges, Danielle Vanhoenacker-Janvier

Synthetic Rain Models and Optical Flow Algorithms for Improving the Resolution of Rain Attenuation Time Series Simulated From Numerical Weather Prediction

Mojtaba Razavian¹ , Claude Oestges¹, and Danielle Vanhoenacker-Janvier¹

¹ICTEAM Institute, Université catholique de Louvain (UCLouvain), Louvain-la-Neuve, Belgium

Abstract New generation of satellite system communication is moving toward frequencies above 20 GHz and non-geostationary satellites. In order to guaranty the quality of service, specific Fade Mitigation Techniques have to be applied, like Advanced Coding and Modulation (ACM). In order to accurately design ACM, time series of attenuation should be used. As there are no measurements available, the simulation of attenuation times series for non-geostationary earth-space links becomes critical. This paper presents a model consisting in a combination of a Numerical Weather Prediction model (Weather Research and Forecasting), a synthetic rain cell model MultiEXCELL and Optical Flow techniques. It gives an efficient method to generate more realistic rain attenuation time series. Long-term CCDF statistics of simulated attenuation data are validated by comparison with the Alphasat measurement data over 2 years at Louvain-la-Neuve ground station.

1. Introduction

Although Earth-Space satellite communications are already using millimeter-wave bands for broadcasting, broadband services and Earth observation data download, there is always a push to use higher frequencies and higher data rates. The Ka and Q/V bands are attractive from the point of view of the frequency bandwidth that can potentially be used. However, the increased degradation due to rain and clouds necessitates the use of specific techniques to ensure the capacity, availability, and quality of service of the data transmission. The classical Fade Mitigation Techniques (FMTs) are power control, site diversity, satellite diversity (Gallinaro et al., 2005). More specific ones must however be used for millimeter-wave transmission, like Advanced Coding and Modulations (ACMs), the dynamic modification of the scheme for data encoding to counteract the received signal attenuation conditions. An accurate design of ACM necessitates the knowledge of time series of the received signal at the frequency and location of interest.

In the absence of experimental propagation data measured on the receiving site, the ability to predict time series of attenuation is important, both for individual Return Channel Satellite Terminals (RCSTs) and for the systems, and second for real-time resource management of the systems (Castanet et al., 2003). Radio wave propagation above 10 GHz is strongly influenced by the troposphere, mainly by rain and clouds. Rain attenuation has been extensively studied in the past, and much effort has been devoted to develop models capable of predicting annual rain attenuation statistics (Bryant et al., 2001; Capsoni et al., 2009; ITU-R P.618-13, 2017). ITU-R proposes widely used models for complementary cumulative distribution (CCDF) of attenuation (ITU-R P.618-13, 2017), fade slope and duration (second-order models) (Recommendation ITU-R P.1623-1, 2003), etc., as well as time series (ITU-R P.1853-2, 2019), for geostationary satellites. For non-geostationary satellite, a model is proposed for the CCDF of attenuation at a given location (ITU-R P.618-13, 2017). It has however never been tested against real measured data. Moreover, there are no second-order models available for non-geostationary satellites (fade slope or fade duration), nor models for generating time series.

1.1. State-Of-The-Art of NWP-Based Propagation Impairments Simulator

All the statistical models are based on measurements at fixed elevation angle and fixed location. Obviously, these models cannot provide details of rain in the full three-dimensional environment surrounding a receiving station: these models are independent of azimuth. Meteorological radar and Numerical Weather Prediction (NWP) models seem to be the only good tools, capable of providing complex information on the structure of rain that is needed to simulate the attenuation for a non-geostationary link. Meteorological output parameters of

NWP models are used for about 15 years (Hodges et al., 2006), to generate time series and CCDF of attenuation at locations all over the world. In the frame of an ESA project (ESA/ESTEC contract 105326, 2015), Jeannin and co-authors (Jeannin et al., 2014; Outeiral García et al., 2013) developed a simulator able to generate propagation impairments time series for LEO satellites as well. The simulator is built around the Weather Research and Forecasting (WRF) model and its originality resides in the use of the output parameters of WRF provided in volume, to calculate the attenuation on the earth-space link. The WRF resolutions used in the method of Jeannin et al. (2014) are typically 2 km horizontally and 5 min in time. The ability of the model to reproduce CCDF of attenuation has been shown for Earth-Space geostationary links. Despite a poor instantaneous correlation in time and space, due to the use of WRF in prediction mode, the simulation of one year or more of CCDF of attenuation shows a good statistical agreement with experimental data, with an error <2 dB, at 20.2 GHz for ASTRA-3B site diversity links in the South of France, for a 1-year period mostly in 2014 (Fayon et al., 2017).

Applications of the NWP-based propagation impairments simulator to FMTs are proposed by Jeannin and Dahman (2016) for earth observation data downlink using ACMs, by Jeannin et al. (2016, 2019) for smart gateways switching and for site diversity. Tentative for predicting the scintillation using NWP models has also been proposed by Pereira et al. (2014) and Marziani et al. (2019).

An extensive validation of the method has been undertaken in the PhD thesis of L. Quibus (Quibus, 2020; Quibus et al., 2019), comparing the output of two NWP models, various WRF models for clouds at various locations and comparison with radar-derived rain attenuation over periods going from 5 to 10 years.

1.2. Present Limitations of the NWP-Based Propagation Impairments Simulator

Most of the results present in the literature are limited to geostationary links. Some non-geostationary cumulative statistics have been produced, but with a limited extent. One of the main limitation is the coarse resolution of the simulator in time and space.

The time resolution of the output of NWP models is limited by the computing time and the storage volume of the output results. In most of the applications described in the previous section, the output meteorological parameters are stored every 5 min, this makes about 2 TB for 1 year simulation data. Going down to 1 min is feasible for a limited duration, for example, a few months, but not for a year or more. If 5 min is reasonable to represent the evolution of the gases, the rain rate, and to a less extend the cloud attenuation, can vary rapidly within that period.

The spatial resolution depends on the NWP model itself. NWP models solve a set of discrete partial differential equations describing the movement and thermodynamic state (pressure, temperature, humidity) of the moist air on a 3D grid. Horizontally to the Earth surface, the resolution ranges from tens of kilometers for larger domains to about 1 km for smaller ones. The practical constraints on the dimensions of the simulation domains mean that some phenomena cannot be directly resolved by the equations, they are supplemented by parametrization, such as for phase changes typically present in clouds. These parametrizations are valid in a limited range of dimensions. Reducing the grid size imposes to add a more effective model, for example, for clouds and to introduce new small scale effects not taken into account for a coarse resolution. The typical resolution used for NWP-based propagation impairments simulator is 1 or 2 km. If this not a problem for gases and widespread clouds, it becomes critical for convective clouds (cumulus and cumulonimbus) and for rain. The rain rate obtained is a mean value over the grid surface ($1\text{--}4 \text{ km}^2$).

Finally, NWPs require initial and boundary conditions for their partial differential equations. The state of the atmosphere and its surface must be first reconstituted from available observations during a data assimilation process. These observations have a limited resolution, for example, the ECMWF ERA-5 and ECMWF ERA-INTERIM databases provide the horizontal resolution of 0.28° (31 km) and 0.75° (80 km), respectively.

Based on the limited resolutions in time (about 5 min) and space (about 1 km) indicated above, it is clear that WRF alone cannot achieve the resolution required for an accurate representation of the rain attenuation. This paper proposes a new method, combining WRF with MultiEXCELL rain model and Optical flow, to reach this goal.

1.3. Summary of Contributions

The model presented in this paper generates a high resolution time-series of attenuation, with an emphasis on rain attenuation time series. The main contributions are:

1. Merging MultiEXCELL model with the output of NWP data to improve the spatial resolution of the rainfall rate.
2. Using Optical flow algorithms to detect the horizontal motion of rain cells and generate rain maps every minutes to increase time resolution.
3. Combining MultiEXCELL and Optical Flow to improve space and time resolution of attenuation due to rain.
4. Validation of the model using attenuation measurements from Louvain-la-Neuve Alphasat station.

1.4. Content of the Paper

Section 2 briefly describes the setup configuration of WRF software. The rainfall rate issued from WRF is used in MultiEXCELL model in Section 3 to produce the high resolution synthetic rain events. Section 4 proposes the use of Optical Flow to improve the time resolution of rain events maps. Finally, Section 6 presents the test of the overall model, by comparing the CCDF of the attenuation time series simulated with the new model, with WRF and the attenuation measurements made at the Louvain-la-Neuve Alphasat ground station.

2. Numerical Weather Prediction for Radio Wave Attenuation Simulation

A NWP software predicts the meteorological parameters (e.g., rain, clouds, wind, humidity, ...) by solving numerically the equations of fluid mechanics, representing the evolution of the atmosphere. NWPs are a very complex processes and include many subprocesses at different temporal and spatial scales. NWPs operate at Global (worldwide atmosphere and surface) scales, Regional (e.g., Western European) scales, or local scales. In this application, the Regional model is used. As the Regional model does not benefit from the closed system and periodic boundary conditions obtained by considering the entire Earth, the boundary conditions must be specified externally, using global models output as ECMWF data sets. In this work, the WRF (WRF V4.2) software by NCAR (Skamarock et al., 2021) will be used. More specifically, the Advance Research WRF (ARW) solver (NCAR, 2022), is the main model exploited for the simulations of propagation impairments.

In order to have a reasonable space resolution for Earth-Space link attenuation simulation, WRF will be run in three nested domains, d01, d02, and d03 with a horizontal grid size of 18, 6, and 2 km, respectively. Each domain has 79×79 points from east to west and south to north and 50 points in vertical levels from surface up to 50 hPa pressure top. Figure 1 shows the equivalent domains with the Lambert Conformal Conic map projection, centered in Louvain-la-Neuve, Belgium.

WRF works in daily runs and its configuration is as follows.

- Initialization data: ECMWF ERA-5 analysis (0.25°) every 6 hr.
- Vertical coordinates: 50 automatic vertical levels, 50 hPa pressure top.
- Lead time: 6 hr
- Run time: 12 hr
- Integration time step: 90, 30, and 10 s for domains d01, d02, and d03, respectively.
- Water microphysics: WRF single-moment 6 (WSM6)
- Cloud physics: Tiedtke (d01, d02), called at each time step, and no cumulus model for inner domain (d03).
- Surface layer physics: revised MM5 Monin-Obukhov scheme.
- Planetary boundary layer physics: Yonsei University (YSU) scheme, called at each time step.
- Soil layer physics: unified Noah land-surface model, four layers.
- Diffusion and damping: second-order diffusion on coordinate surfaces, Rayleigh damping with damping coefficient (inverse timescale) 0.2 Hz.
- Radiation physics: RRTM schemes for long-wave and Dudhia scheme for short-wave radiations.

Other parameters are left to their default values. More information and how to choose all options is fully described on the NOAA, Earth System Research Laboratory website (NOAA, 2022).

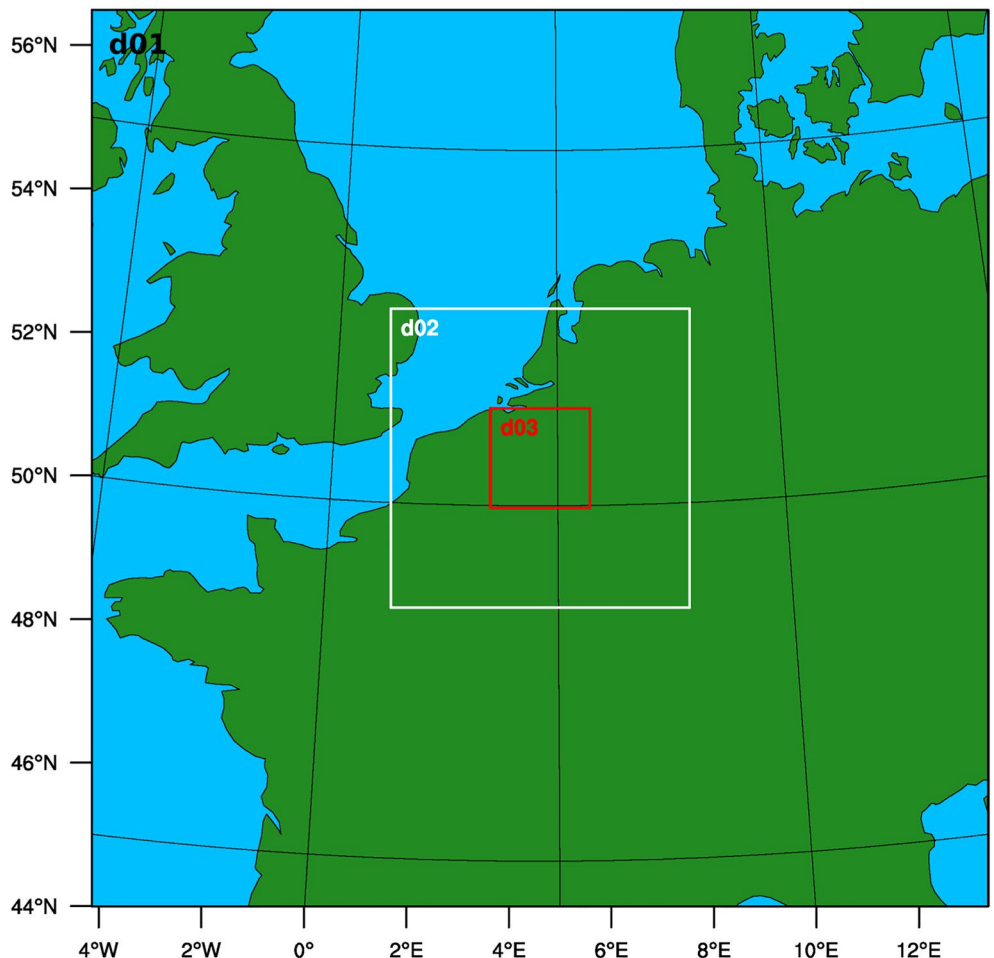


Figure 1. Domains configuration of Weather Research and Forecasting with horizontal scales of 18, 6 and 2 km, respectively, for d01, d02, and d03. The map projection is Lambert Conformal Conic.

Finally, the attenuation on the desired Earth-Space path (geostationary or not) is calculated by using the ITU-R recommendations (ITU-R Recommendation P.838-3, 2005; ITU-R Recommendation P.840-7, 2017) and the output of WRF, such as rain rate, cloud liquid water content, pressure, temperature and height. Further details on the use of WRF for the simulation of attenuation on Earth-Space link can be found in Jeannin and Dahman (2016) and Quibus et al. (2019). The spatial resolution obtained is 2 km and the time resolution, corresponding to the time between two successive WRF output stored, is 5 min. Increasing the space or time resolution would lead to a dramatic increase in running time and data storage volume.

3. MultiEXCELL Rain Model for Improving Spatial Resolution

The spatial features of the rain field at mid- and large-scale are investigated through their natural aggregating process by Luini and Capsoni (2011) and a model called MultiEXCELL has been introduced. In this model, the clusters (aggregates) of cells in terms of distance between individual cells, number of cells per aggregate and rain rate threshold are characterized. In this paper, the output of WRF model will be used to feed initial input data (rainfall rate) to the MultiEXCELL model, instead of using radar data. As the MultiEXCELL model uses a mathematical representation of the rain cells, the spatial resolution of 2D-rain attenuation maps can be increased effectively, to grid cells of about 100 m².

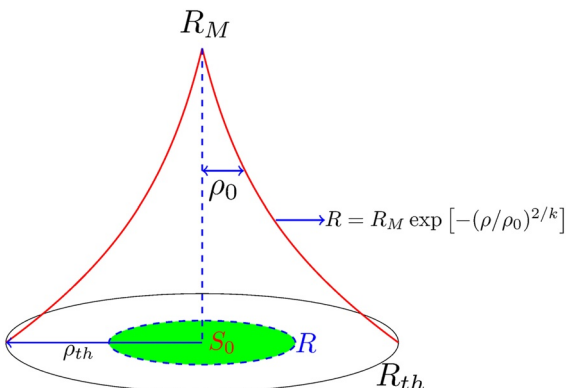


Figure 2. Typical rain cell in MultiEXCELL model.

3.1. MultiEXCELL Rain Model

The rain cell is defined as a spatial region where the rainfall rate exceeds a specified intensity threshold (e.g., 1 mm/hr). The main objective of the MultiEXCELL model is the optimal reproducibility of the cumulative distribution of point rain rates $P(R)$. The theoretical representation of rain rate for a single cell has an exponential form:

$$R(\rho) = R_M \exp [-(\rho/\rho_0)^{2/k}], \quad (1)$$

where R [mm/hr] is the rain rate, ρ [km] is the distance from the cell center, R_M [mm/hr] is the maximum rain rate occurring at the center of the cell, and ρ_0 [km] is the equivalent radius for which $R = R_M/e$ (see Figure 2). In fact, Equation 1 identifies multiple profiles, depending on k chosen. The shape factor, $k = 1$, $k = 2$ or $k = 3$, respectively define Gaussian, exponential or hyper-exponential cell profiles. Capsoni et al. (1987) stated that the exponential profile ($k = 2$) fits the best with the experimental results.

Model definition requires identifying R_M and ρ_0 parameters accurately. They can be estimated by imposing suitable descriptors to be the same in the NWPs data and in the model cell.

The two first descriptors chosen for a rain cell are (a) the rain cell area A_{th} , and (b) the average rain rate \bar{R} (Luini & Capsoni, 2011). These quantities are mathematically represented as

$$A_{th} = \pi \rho_{th}^2 = \pi \rho_0^2 \ln^k (R_M / R_{th}), \quad (2)$$

$$\bar{R}_{th} = \frac{1}{A_{th}} \int_0^{\rho_{th}} R(\rho) 2\pi \rho d\rho = \frac{k R_M}{\ln^k (R_M / R_{th})} \gamma(k, \ln(R_M / R_{th})), \quad (3)$$

where R_{th} is the minimum level of rain rate to define a rain cell (e.g., 1 mm/hr), ρ_{th} is the maximum radius of the rain cell equivalent to R_{th} (see Figure 2). $\gamma(s, x)$ is the lower incomplete gamma function:

$$\gamma(s, x) = \int_0^x t^{s-1} e^{-t} dt = x^s \Gamma(s) e^{-x} \sum_{k=0}^{\infty} \frac{x^k}{\Gamma(s+k+1)}. \quad (4)$$

The left side of Equations 2 and 3 are calculated numerically from NWPs rainfall rate, while the expressions on the right side are calculated for synthetic cells whose properties are defined by Equation 1. Solving these equations gives the two main parameters R_M and ρ_0 while assuming a fix value of k .

During the numerical calculation, many combinations of parameters R_M and ρ_0 are found. The most appropriate pair can be selected by using more advanced descriptors of NWPs data and synthetic rain cells. The peak rainfall rate (\bar{R}_{max}), the root-mean-square of the rain rate R_{rms} and the cell dynamics R_{dyn} are suitable descriptors. \bar{R}_{max} descriptor writes as (Luini & Capsoni, 2011).

$$\bar{R}_{max} = \frac{1}{A_p} \int_0^{\bar{\rho}} R(\rho) 2\pi \rho d\rho = \frac{k \pi R_M \rho_0^2}{A_p} \gamma(k, \bar{x}) \quad (5)$$

$$\bar{x} = \left(\frac{\bar{\rho}}{\rho_0} \right)^{2/k} \quad (6)$$

$$\bar{\rho} = \sqrt{A_p / \pi}, \quad (7)$$

where $\bar{\rho}$ and A_p indicate the equivalent radius and the area of the single pixel (the smallest grid size in the NWP or radar data) where the maximum of rainfall rate occurs (typically the center of each cell; see Figure 3). R_{rms} is defined by:

$$R_{rms} = \sqrt{\frac{1}{A_{th}} \int_0^{\rho_{th}} R^2(\rho) 2\pi \rho d\rho} = \sqrt{\frac{k R_M^2}{2^k \ln^k (R_M / R_{th})} \gamma(k, 2 \ln(R_M / R_{th}))}, \quad (8)$$

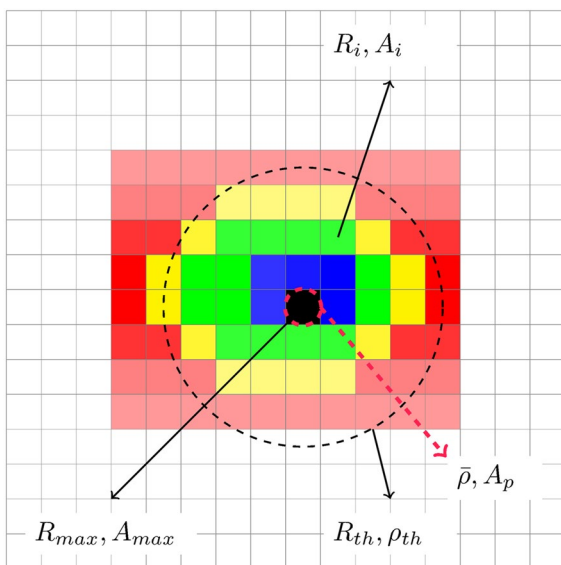


Figure 3. Weather Research and Forecasting and synthetic cell combination.

rain events has confirmed that a termination level of 0.5 mm/hr gives a good accuracy. As it can be observed in the figure, the heavy rain cells are represented more accurately than the light rain. This is due to the fact that the MultiEXCELL model performs better for heavy rain events, as illustrated in Figure 4d.

4. Rain Motion by Optical Flow Algorithm

Improving the temporal resolution of rain attenuation time series can be achieved by rain motion techniques. These techniques can be of two types. First, based on the horizontal movement of rain events alongside with the wind speed and direction. Second, moving of rain events alongside with their displacement between two (or more) consecutive time samples. As the 3D wind speed structures are complex in the rain cell and depend on the altitude, it is practically impossible to find a mean wind speed vector representative for each rain cell. So, the rain cell movement using wind speed cannot be used to produce rain events with high temporal resolution. Then the only remaining option is Optical Flow algorithms.

Optical Flow is a pattern of apparent motion of objects that occurs in a visual scene due to the relative motion between an observer and a scene. For a two-dimensional image (brightness image), we assume that the intensity map $I(x, y, t)$ at location (x, y) and time t will be moved by the spatial displacement $(\Delta x, \Delta y)$, after a Δt time between the two image frames. Most methods that compute optical flow assume that the color/intensity of a pixel is invariant under the displacement; this is called the brightness constancy constraint

$$I(x, y, t) = I(x + \Delta x, y + \Delta y, t + \Delta t). \quad (10)$$

Assuming that the displacement is small, the Taylor series can be used to get:

$$I(x + \Delta x, y + \Delta y, t + \Delta t) = I(x, y, t) + \frac{\partial I}{\partial x} \Delta x + \frac{\partial I}{\partial y} \Delta y + \frac{\partial I}{\partial t} \Delta t + \text{higher-order terms} \quad (11)$$

Assuming a linear scheme for the system, the higher order terms vanish and inserting Equation 10 results into:

$$\frac{\partial I}{\partial x} \Delta x + \frac{\partial I}{\partial y} \Delta y + \frac{\partial I}{\partial t} \Delta t = 0 \quad (12)$$

Dividing the above equation by Δt : gives

where ρ_{th} and R_{th} are introduced earlier and are represented in Figure 3 too. Finally, R_{dyn} is evaluated by

$$R_{dyn} = \frac{\bar{R}_{th}}{R_M} = \frac{k}{\ln^k(R_M/R_{th})} \gamma(k, \ln(R_M/R_{th})). \quad (9)$$

As in Equations 2 and 3, left side of Equations 5, 8, and 9 are calculated from WRF (or radar data) and right side of them are calculated from synthetic rain cells.

3.2. Applying MultiEXCELL to WRF Data

For the detection of individual events, R_{th} above 1 mm/hr is considered as proposed by (Luini & Capsoni, 2011). The pixel with highest rain rate is selected as the center of the first cell, the parameters of the EXCELL rain cell are calculated as indicated in the previous section. A termination level of 0.5 mm/hr is set for the new cell. The next pixel with the highest rain rate outside the first cell is selected and so on, until there is no pixel left with rain rate larger than 1 mm/hr. Special care is taken at the intersection of two rain cells to avoid jumps in the rain rate. Figure 4 represents two examples of original WRF rain rate with their equivalent synthetic rain cells. A parametric simulation and testing of various R_{th} and termination levels on different

rain events has confirmed that a termination level of 0.5 mm/hr gives a good accuracy. As it can be observed in the figure, the heavy rain cells are represented more accurately than the light rain. This is due to the fact that the MultiEXCELL model performs better for heavy rain events, as illustrated in Figure 4d.

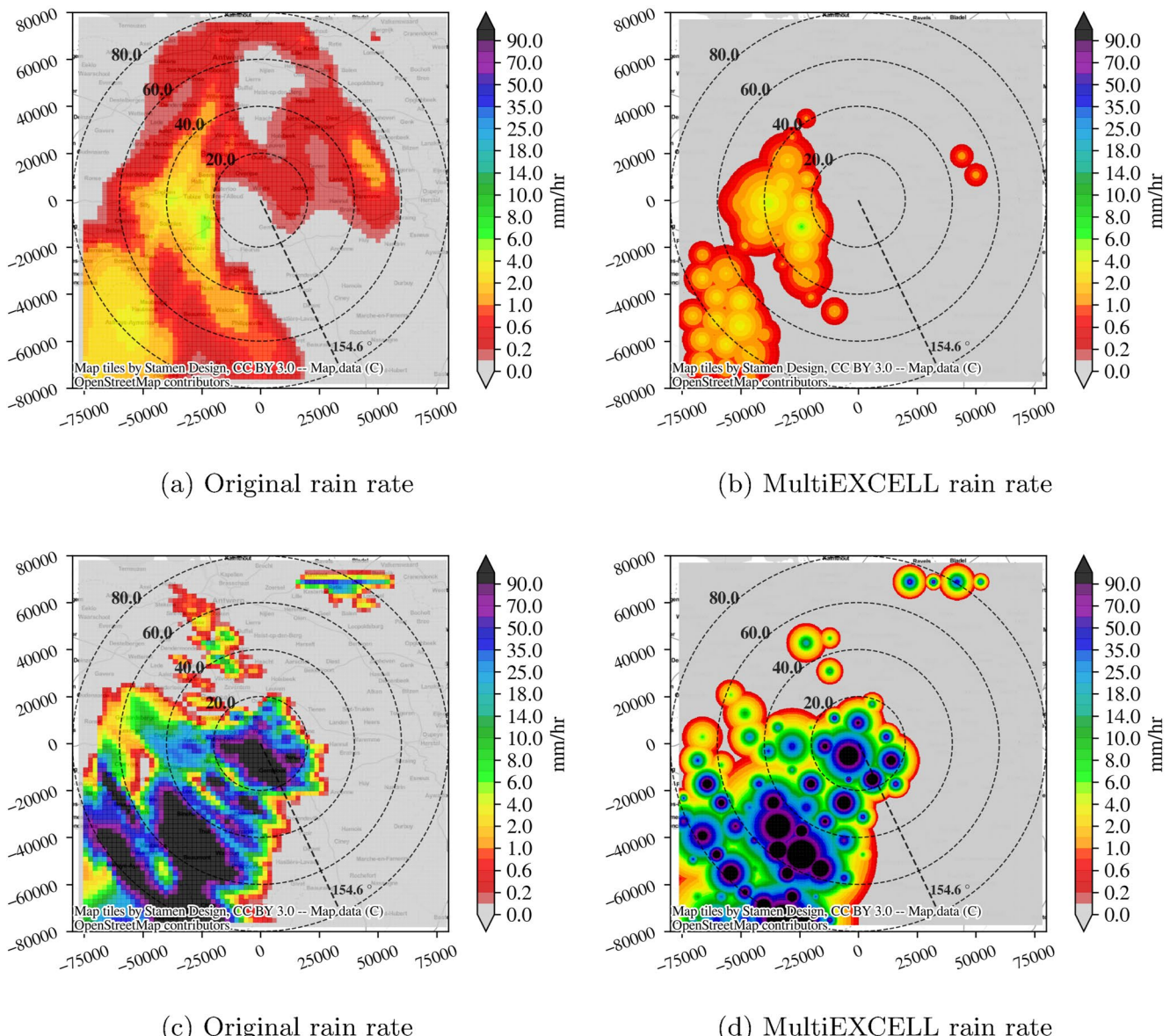


Figure 4. (a and c) show Weather Research and Forecasting original rain rate on 2019-06-05 08:40:00 and 2019-07-27 04:00:00, respectively, in a region centered in Louvain-la-Neuve, Belgium. (b and d) represent the equivalent MultiEXCELL rain rate.

$$\frac{\partial I}{\partial x} u_x + \frac{\partial I}{\partial y} u_y + \frac{\partial I}{\partial t} = 0 \quad (13)$$

where

$$\begin{aligned} u_x &= \frac{\Delta x}{\Delta t} \\ u_y &= \frac{\Delta y}{\Delta t} \end{aligned} \quad (14)$$

are the two components of the optical flow of the voxel (x, y, t) . The $\frac{\partial I}{\partial x}$, $\frac{\partial I}{\partial y}$ and $\frac{\partial I}{\partial t}$ are the derivatives of the image intensity at (x, y, t) for the corresponding components. Equation 13 can be rewritten in the form:

$$\nabla I \cdot \mathbf{u} + I_t = 0 \quad (15)$$

This equation, known as the aperture problem of the optical flow method, is difficult to solve because it has two unknown factors, (u_x , u_y). The unknown parameters can be estimated using a variety of techniques by adding additional conditions to the equation.

The typical measure of the difference between two consecutive image contents is

$$L_1 \text{ norm} = \sum_{k \in S} |T(\mathbf{k}) - \tilde{I}(\mathbf{k} + \mathbf{u}(\mathbf{k}))| \quad (16)$$

$$L_2 \text{ norm} = \sum_{k \in S} [T(\mathbf{k}) - \tilde{I}(\mathbf{k} + \mathbf{u}(\mathbf{k}))]^2 \quad (17)$$

where $\mathbf{k} = [k, l]^t \in Z^2$ are the discrete positions, and $\mathbf{u}(\mathbf{k}) = [u(\mathbf{k}), v(\mathbf{k})]^t$ is the optical flow vector field. $S = \{0, \dots, K-1\} \times \{0, \dots, L-1\}$ is the original plane of the image, T stands for the “template image” and \tilde{I} denotes interpolated “inspection image” intensities, often two consecutive frames in a sequence.

A brief quantitative evaluation of the existing methods in optical flow is done in Barron et al. (1994) and Baker et al. (2011). The TV-L1 method is based on the minimization of the L_1 norm and a regularization term using the total variation (TV) of the flow (Sánchez Pérez et al., 2013). The main features of this method is the capability of considering discontinuities in the flow field, which makes this algorithm more robust than Lucas-Kanade (Besnerais & Champagnat, 2005) method in flow field estimation. Thus, in this paper, the well known model TV-L1 is preferred to find the rain motion flow fields.

Optical Flow algorithm is used for image frames, and some preprocessing of rainfall rate data maps is needed before feeding them to optical flow algorithms. This procedure can be applied to both the original WRF and MultiEXCELL rainfall rates. Since the output of MultiEXCELL model has a high spatial resolution, its use as the input of Optical Flow algorithms is a high time-consuming process. It has then been decided, for analysis and parametrization purpose, to use the original rain rate data of WRF on a 79×79 2D data grid. A problem that showed up was the non-respect of the brightness consistency hypothesis: this problem will be analyzed in the following section.

4.1. Preparation of the Rainfall Rate 2D Maps for Feeding in Optical Flow Algorithm

The first step in preparing the 2D-rain rate data is to transform them to an “image.” The images are defined in many formats. RGB images consist in three layers of 2D matrices, each layer representing the intensity of each main colors, Red, Green, and Blue. Another common image formats is the gray color or brightness images. The gray scaled images include only one layer of 2D data representing the intensity of the brightness, scaled from 0 (black) to 1 (white). Since the rain rate data is a 2D data, the appropriate format in our case is gray scaled or brightness images.

Considering the images sequence I_0 and I_1 containing the rain rate pixels, the normalization is a simple mathematical scaling over the two images.

$$c_1 = \min(I_0, I_1), \quad (18a)$$

$$c_2 = \max(I_0, I_1), \quad (18b)$$

$$I_i^{\text{norm}} = \frac{I_i - c_1}{c_2 - c_1} \quad i \in 1, 2. \quad (18c)$$

Linear normalization introduces a problem. Most of the time, the minimum rain rate is 0 and in case of a heavy rainfall rate occurring in a small portion of the domain, the difference between minimum and maximum rainfall rate reaches 100 mm/hr or even more (e.g., Figure 5) and, after normalization, very low values of rain rate disappear during the image processing. Also, the differences between the peaks of I_0 and I_1 can be important in case of heavy rain events and time steps of 5 min between two images. Figure 5 shows a cross-section of a moving rain event and the final normalization. The blue curve is a cross-section of rain rate distribution at time t and the orange curve is the cross-section of the same rain event after dt . It is displaced horizontally and the intensity of rain rate is increased. It's clear that during the normalization of rain rate, high differences in peak value could exist (Figure 5a).

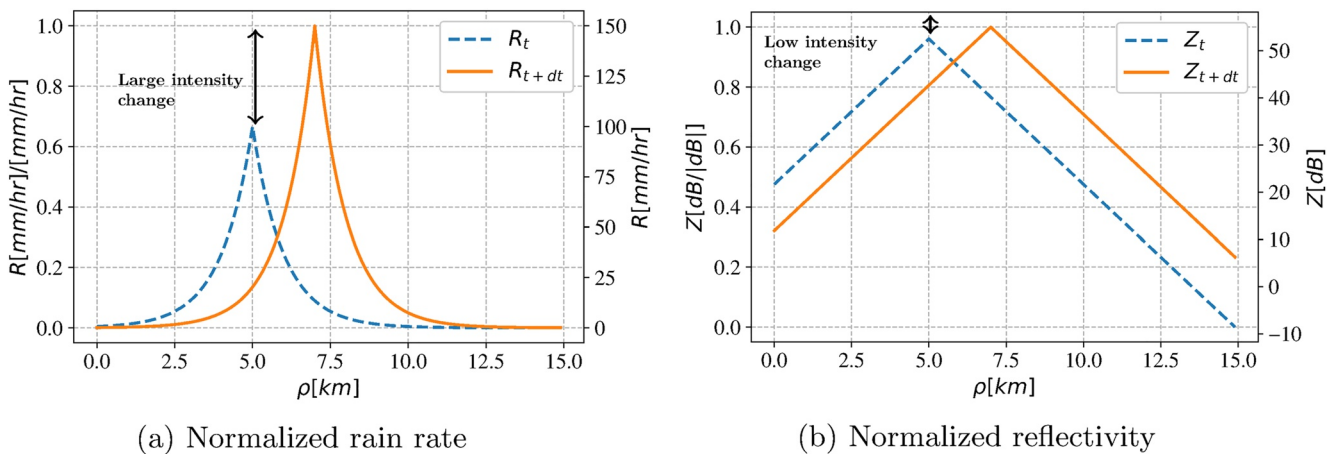


Figure 5. Comparison between the normalized rain rate and normalized reflectivity.

These high difference between two consecutive images does not comply with the brightness constancy constraint in Equation 10. To solve this problem, Heistermann et al. (2013) and Ayzel et al. (2019) propose to use the reflectivity quantity in decibel instead of the rain rate in optical flow algorithm.

$$Z = a R^b, \quad (19a)$$

$$Z_{dB} = 10 \log Z, \quad (19b)$$

where R is the rain rate in mm/hr, $a = 256$, and $b = 1.42$ are the power law coefficients (Ayzel et al., 2019). The reflectivity Z_{dB} is used in Equation 18 as input of optical flow algorithms. Using the normalized reflectivity is a better option, since the reflectivity variation is inversely proportional to rain rate, $\frac{dZ_{dB}}{dR} \propto R^{-1}$. Thus, when using the normalized reflectivity, the rainfall rate images will be mostly considered as a constant solid object, for example, Figure 5b, which is suitable in optical flow algorithms.

Figures 6a and 6b illustrate this concept for two consecutive rainfall rate maps I_0 and I_1 . These are two successive maps of a rain event occurring on 2019-07-27 06:15:00 and 2019-07-27 06:20:00, respectively. The related normalized rain rate and normalized reflectivity are plotted in Figures 6c–6f which again show the importance of using reflectivity instead of rain rate in optical flow algorithms. Figures 6c–6f clearly shows that the normalized reflectivity better obeys the brightness consistency hypothesis than the normalized rainfall rate. So, the lower rain rate values and lower intensities are taken into account more effectively in Figures 6e–6f.

4.2. Rain Rate Registration

The preprocessed images, in Figures 6e–6f, are ready to be fed to the TV-L1 optical flow algorithm. Figure 7a depicts both magnitude and direction of the flow field ($\mathbf{u}(k)$), which is the main outcome of optical flow algorithm (Sánchez Pérez et al., 2013). Figure 7b represents the interpolated inspection image $\tilde{I}_0(k + \mathbf{u}(k))$. In image processing, the interpolation of the inspection image is called warping and the result of warping (e.g., $\tilde{I}_0(k + \mathbf{u}(k))$) is called registered image.

The L_1 norm of this registration in Figure 7c shows that the majority of high deviations occur at the border of the image solid objects (rain events). The remaining deviation is due to the changes in image intensity, in our case rain rate. This last point becomes important when there is a large change in image intensity. Then one more step is needed for the compensation of the intensity variation. Section 4.3 explains how to solve numerically the changes in image intensity in the optical flow algorithms.

The purpose of image registering and optical flow fields estimation is to fill the gap between two successive images of rainfall rate: I_0 at $t = 0$ and I_1 at $t = 1$ where t represents the normalized time period. Considering the image sequence

$$I_0, \dots, I_{i-1}, I_i, I_{i+1}, \dots, I_1, \quad (20)$$

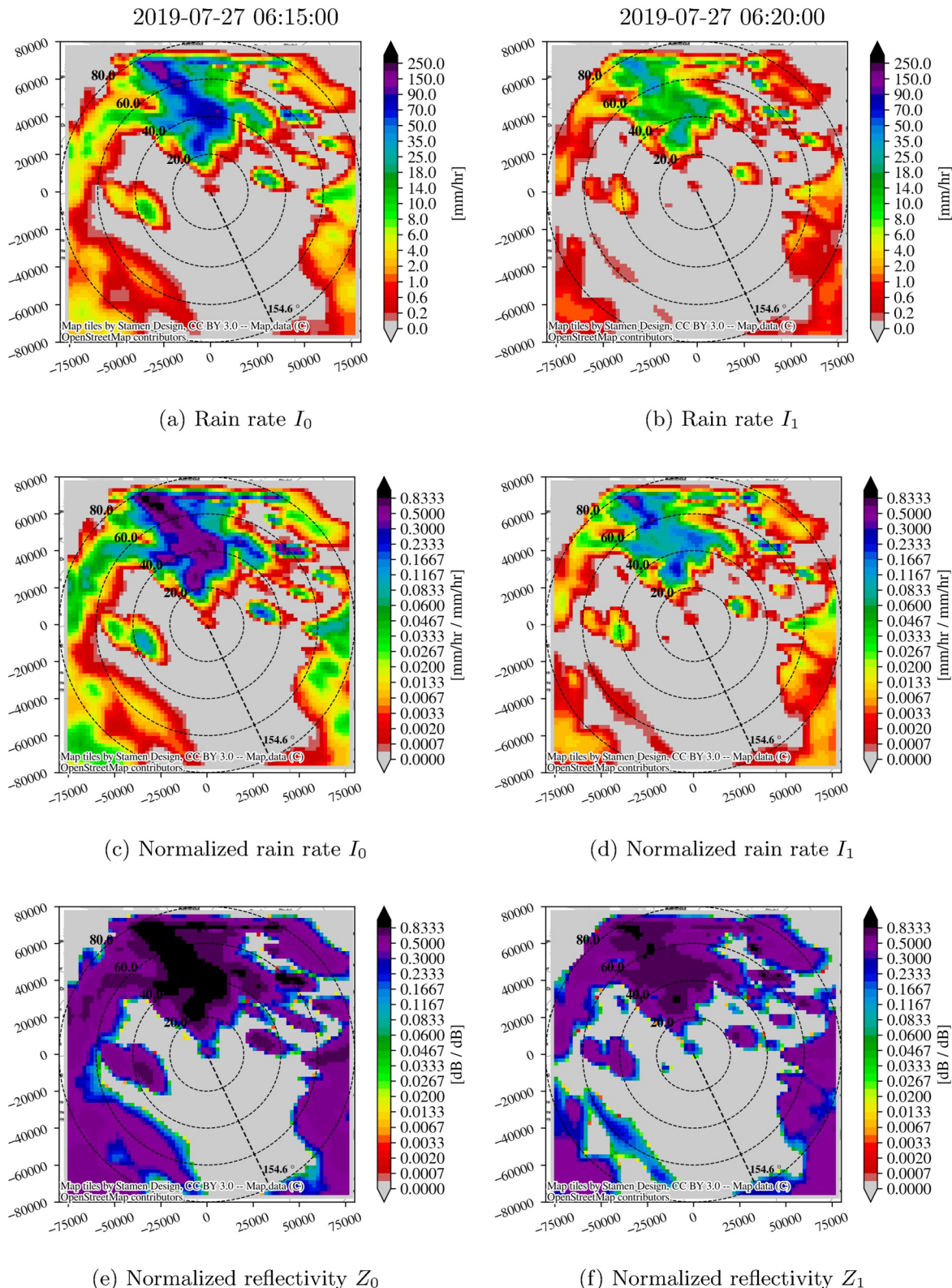


Figure 6. Transformation of rain rate to normalized reflectivity to be fed into optical flow algorithms. The ground station is in Louvain-la-Neuve.

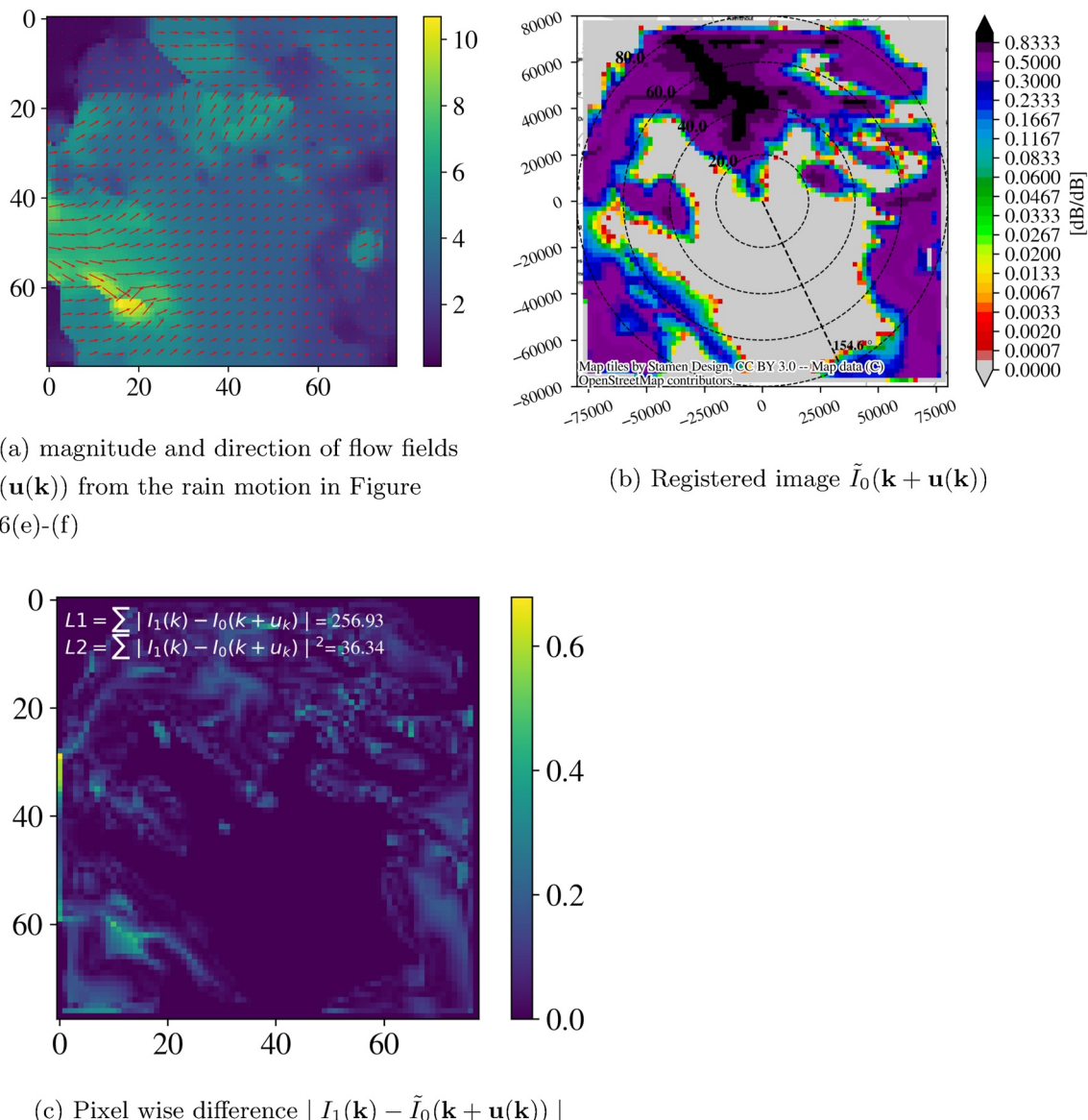


Figure 7. Normalized reflectivity registration and warping using optical flow algorithms (TV-L1). (a) shows the flow field vector, (b) the registration of $\tilde{I}_0(\mathbf{k} + \mathbf{u}(\mathbf{k}))$ using the flow fields vectors $\mathbf{u}(\mathbf{k})$, (c) the error values L_1 norm between the registered image and target image for the rain event of 2019-07-27 06:15:00 in Louvain-la-Neuve.

assuming that the trajectory is linear between two consecutive images I_0 and I_1 and utilizing the displacement pattern $\mathbf{u}(\mathbf{k})$, the flow fields for the motion of the objects at the time t_i are

$$\mathbf{u}_i = t_i \times \mathbf{u}, \quad 0 \leq t_i \leq 1, \quad (21)$$

where \mathbf{u} is the optical flow field, for example, Figure 7a. So each of the I_i is calculated by warping and utilizing the \mathbf{u}_i .

$$I_i = \tilde{I}_0(\mathbf{k} + \mathbf{u}_i). \quad (22)$$

Figures 6a and 6b illustrate the evolution of the rain rate between two output of WRF, 5-min apart. The rain motion sequence with the temporal resolution of 1-min is depicted in Figure 8. This Figure represents the rain motion as the normalized reflectivity. Each sub-image of rain rate is recovered by inverting the normalization in Equations 18 and 19.

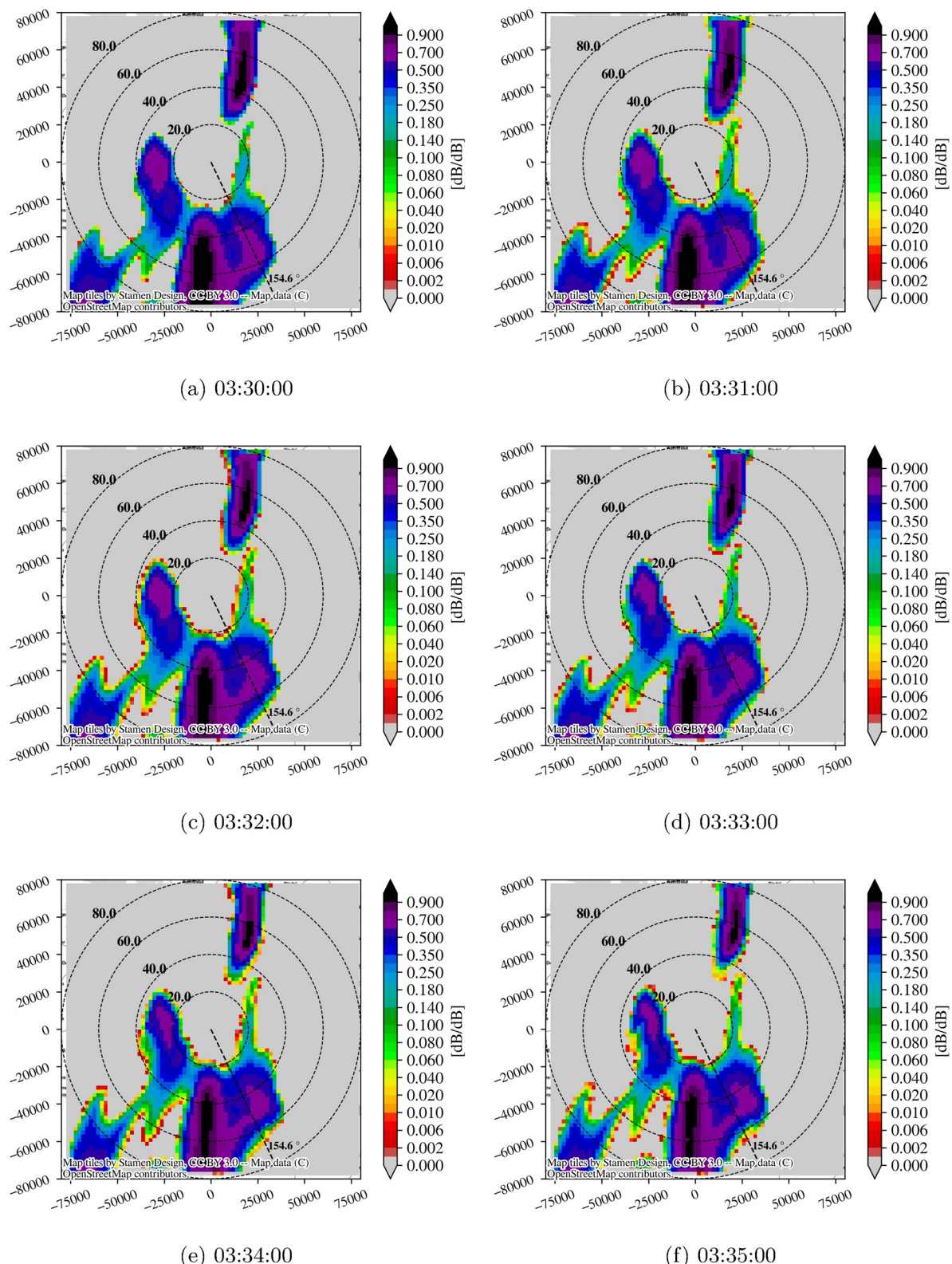


Figure 8. Rain motion using optical flow method from 2019-06-05 03:30:00 to 2019-06-05 03:35:00 with temporal resolution of 1-min. The figures are normalized reflectivity for which the equivalent rain rate is retrieved by using the inverse procedure of Equations 18 and 19.

Figure 8 includes the time evolution of rain events in which the intensity is mostly constant, and the rule of brightness constancy is valid. This case is a simple case in which the motion is smooth during a 5-min period. To check the capability of optical flow in a case of complex motions and with degradation or deformation in the rain event, another example is studied. Figure 9 represents the rain rate for the time period 2019-06-05 06:00:00 to 2019-06-05 06:05:00 with the center at Louvain-la-Neuve. This rain event illustrates both deformation and intensity change. The motion detection of the rain event is well estimated, but there is still a problem with the intensity. Figures 9e and 9f clearly show that there is a jump in the rain intensity from 06:04:00 to 06:05:00. Optical flow algorithms are not able to restore intensity changes. This intensity change over the time period is numerically solved in Section 4.3.

4.3. Rain Intensity Correction in Optical Flow

As discussed earlier, the brightness constancy constraint in optical flow is a must. On the other hand, some rain events change a lot during small time periods (e.g., 5 min). The effect of large changes in rain rate was already reduced by using the normalized reflectivity in optical flow algorithms. But as it can be seen from Figure 9, there is still a large intensity variation of rain rate in complex situations.

Solving the intensity discontinuity can be done numerically by measuring the intensity deviation after registration:

$$\Delta I = I_1(\mathbf{k}) - \tilde{I}_0(\mathbf{k} + \mathbf{u}(\mathbf{k})). \quad (23)$$

and adding this difference gradually to the registered images using

$$\tilde{I}_0(\mathbf{k} + \mathbf{u}_i) \leftarrow \tilde{I}_0(\mathbf{k} + \mathbf{u}_i) + t_i \times \Delta I, \quad (24)$$

where \mathbf{u}_i and t_i are given in Equation 21. The added term in Equation 24 is a linear intensity correction in the lead step times, which at the end causes a smooth change in the intensity of the images. The application of this procedure to Figure 9 is presented in Figure 10. This figure clearly shows the smooth transition of rain intensity between the successive images. The details of this transition and the effect of rain intensity correction will be shown later in Section 5.

5. Simulation of Attenuation Time Series

The first step to generate time series of attenuation is the calculation of 3D specific attenuation of clouds and rain in Azimuth-Elevation-Range coordinates centered on the satellite ground station, using the ITU-R models referenced in Section 2. In the case of rain attenuation, the rain rate is a surface parameter. To obtain a 3D parameter, the rain rate is assumed to be constant in height up to the level of the 0°C isotherm. The rain rate is assumed to be 0 above the 0°C isotherm height. For cloud attenuation, the pressure, temperature and cloud liquid water content are already in 3D. The second step is the integration of the specific attenuation (γ) over the slant range along the earth-satellite link. For a GEO satellite, the azimuth and elevation are constant. So the attenuation is calculated using bilinear interpolation in azimuth and elevation. For a non-geostationary satellite, the Azimuth-Elevation attenuation maps are calculated as well as the azimuth and elevation of the satellite in function of time.

An example of rain and cloud attenuation is simulated using the model proposed, and a short period is plotted in Figure 11 for a geostationary earth-space link in Louvain-la-Neuve ([lat,lon] = [50.67,4.61]) at 39.4 GHz with an azimuth of 154° and an elevation of 30°. As WRF is running as a prediction model, it does not give the exact rainfall rate at a given place and on a given time. This explains the difference in peak positions and intensity. The simulation curves give the output of WRF model alone and the new WRF + MultiEXCELL and Optical flow. Figure 11a shows the attenuation due to gases, clouds and rain with 5-min resolution, for WRF alone and for WRF + MultiEXCELL. The curves are simply linear interpolation between the simulation points. The time series of cloud attenuation is interpolated to have the same resolution as rain attenuation. Since its time variability is smaller than the one of rain attenuation, linear interpolation is a good solution to increase the temporal resolution of cloud attenuation.

Figure 11b shows the contribution of rain and cloud in two models of MultiEXCELL and WRF rain rates, which the rain rates have been processed through the optical flow algorithm.

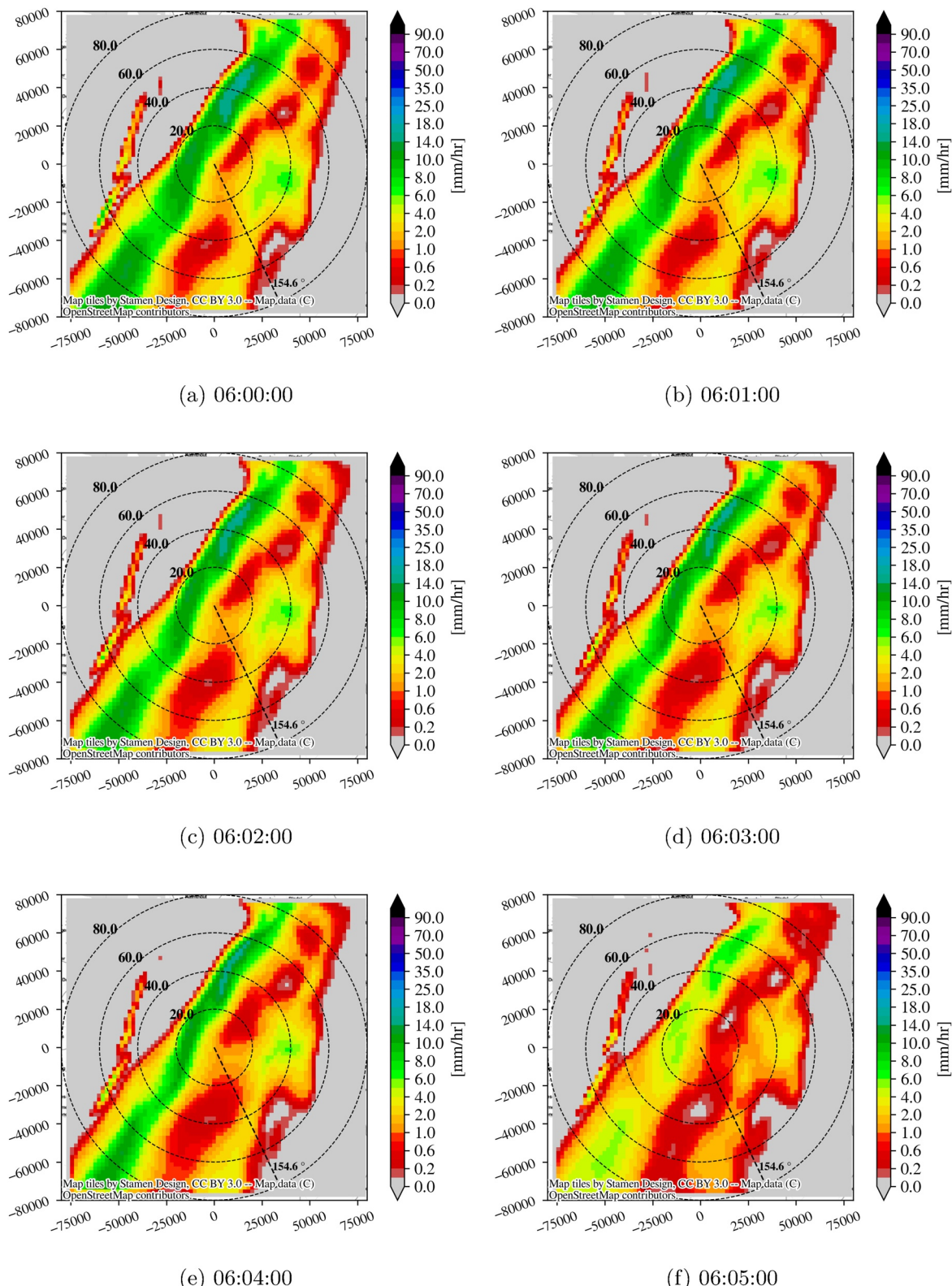


Figure 9. Rain motion using optical flow method in 5-min at the dates 2019-06-05 06:00:00 and 2019-06-05 06:05:00 with temporal resolution of 1-min. The ground station is at Louvain-la-Neuve.

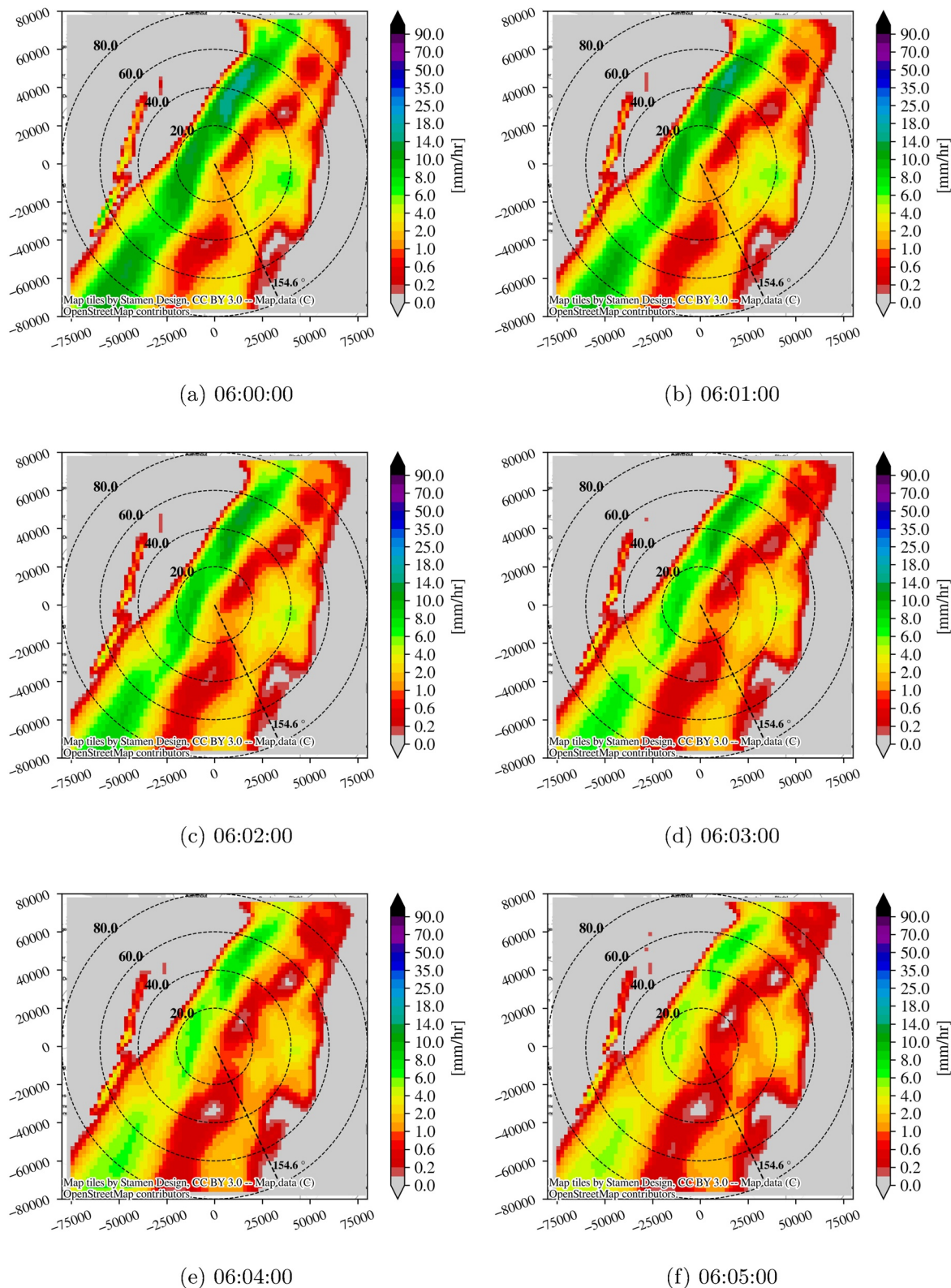


Figure 10. Rain rate intensity correction after registration in optical flow. The event is on 2019-06-05 at Louvain-la-Neuve ground station.

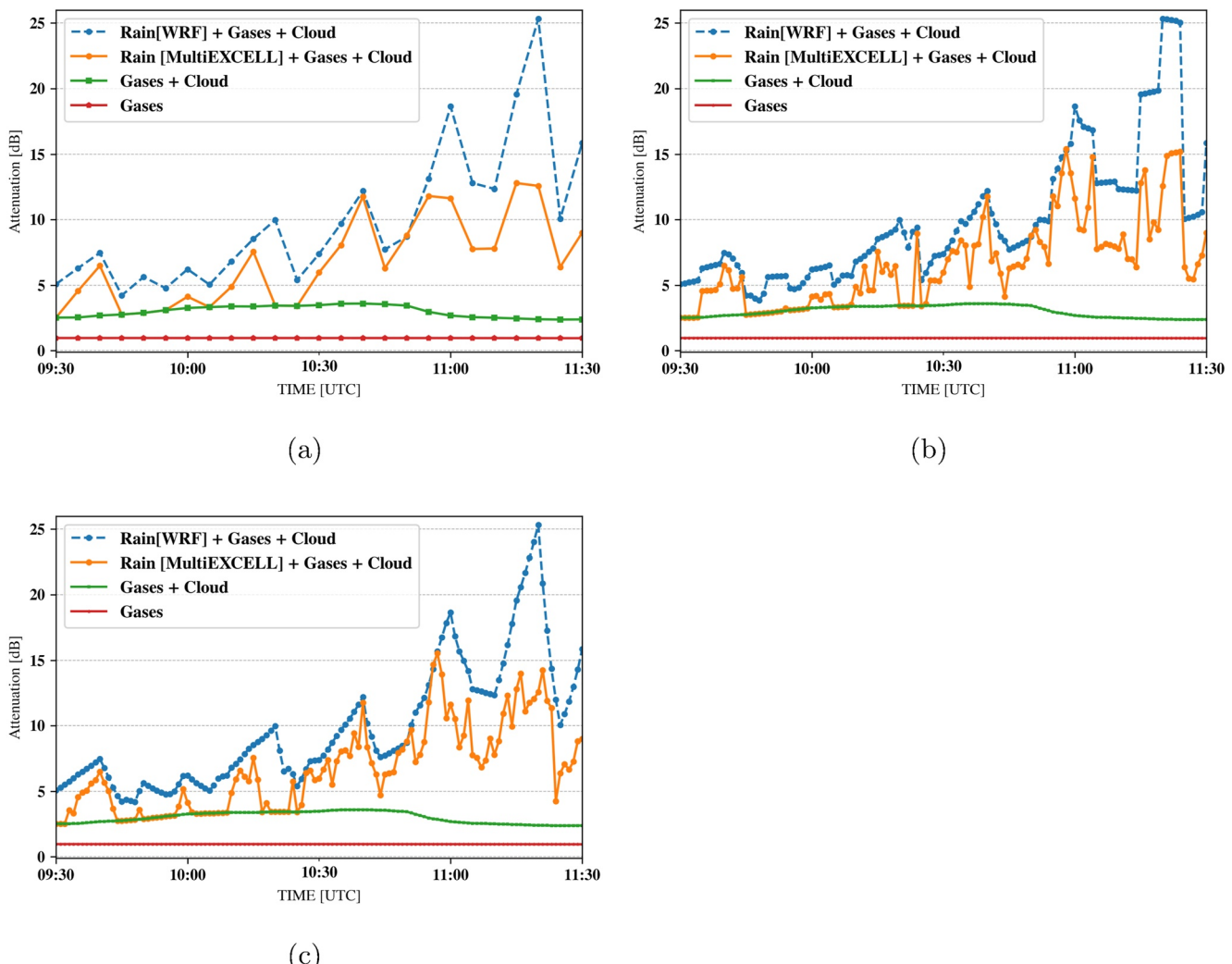


Figure 11. Example of WRF-derived attenuation time series at 39.402 GHz for Louvain-la-Neuve, at 30° elevation and 154.6° azimuth, on 2018-09-23. (a) Time Series with 5-min resolution, (b) Time series with the sample rate increased to 1-min using optical flow without intensity correction for rain rate, and (c) Time series with the sample rate increased to 1-min using optical flow with intensity correction for rain rate.

The graph of WRF in Figure 11b has discontinuities every 5-min because the invariance of rain rate intensity every 5-min and during the optical flow has not been solved yet. As noticed before, the optical flow accuracy degrades in case of large changes in intensity of successive image sequences. Figure 11c shows the time series of attenuation after rain intensity correction procedure discussed in Section 4.3.

6. Validation of the Model

The validation of the model can only be performed for a geostationary satellite. The yearly CCDF of excess attenuation calculated with the new model is compared with the CCDF of copolar attenuation of Alphasat beacon data measured at Louvain-la-Neuve, Belgium. Two years of copolar data at 19.7 and 39.4 GHz, measured at the earth-station of Louvain-la-Neuve in 2018 and 2019, have been processed. The cloud and rain events have been tagged and, in the absence of radiometer, only the excess attenuation has been evaluated.

Figure 12 represents the CCDF of excess attenuation calculated using WRF alone, using WRF, MultiEXCELL, and optical flow with rain intensity correction. The figure displays the statistics for 1-min time series resolution. The new model (MultiEXCELL) nicely estimates the long-term statistics for the time percentages above 0.1%. The new model fails to exactly reproduce the statistics for time percentages less than 0.1% of the year, however

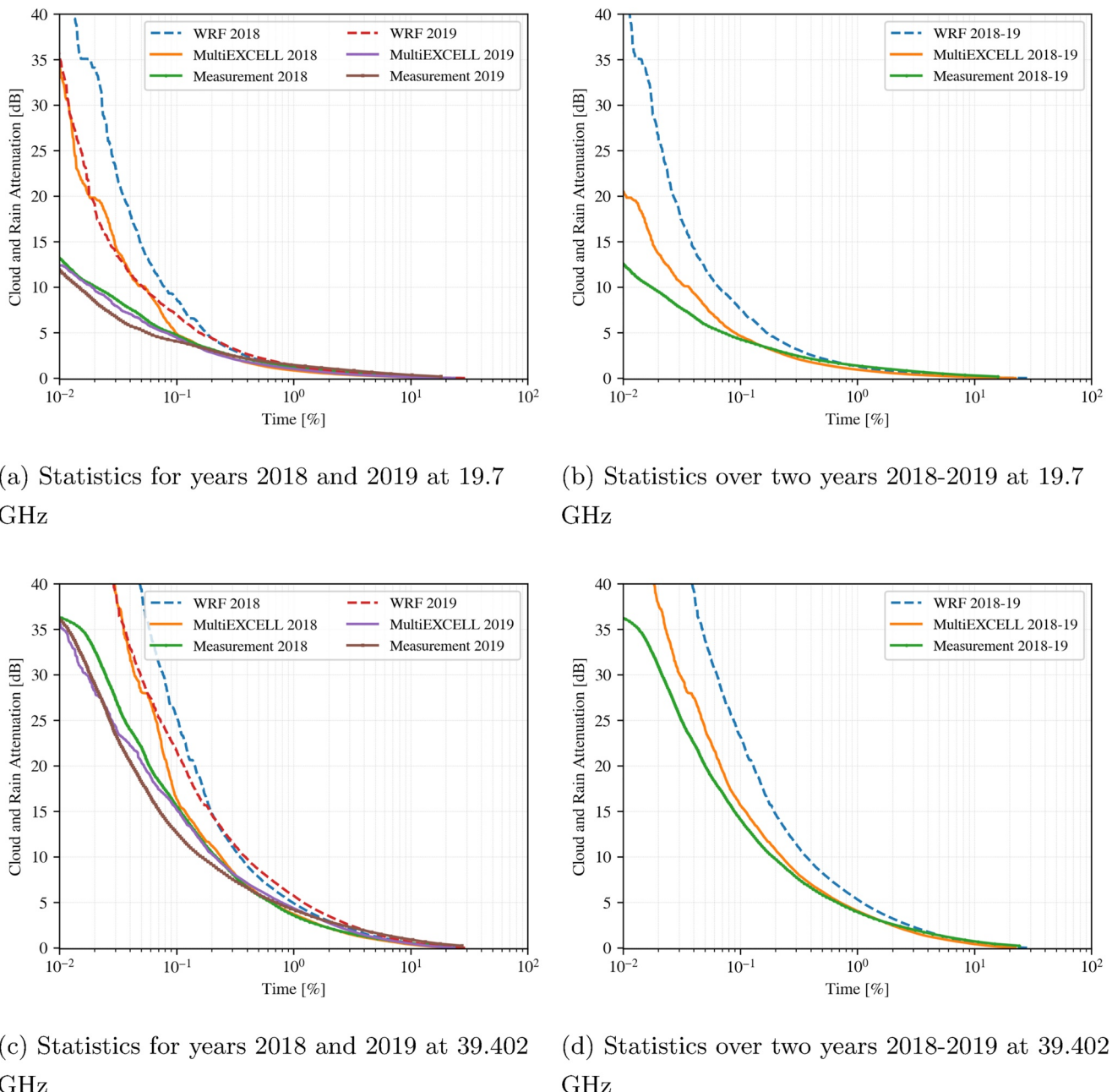


Figure 12. Comparison between Rain + Cloud attenuation CCDFs of attenuation simulated using WRF, WRF + MultiEXCELL rain rate and CCDF of attenuation measurement, at 19.701 and 39.402 GHz, 30° elevation and 154° azimuth, in Louvain-la-Neuve in 2018, 2019, and for both years.

the estimation is still better than original WRF data. It has to be mentioned that the attenuation saturates for values of attenuation higher than 35 dB, which corresponds to time percentages of 0.01%–0.1%. This corresponds to the dynamic range of the measuring station.

Being given a simulated data $A(p)$ of a propagation impairment and a reference data (here the measurement) $A_m(p)$ for that same impairment, the error metric described in ITU-Radio communication Study Groups (2016) is used. The attenuation is tested at a fix set of probability levels

$$S_i = \frac{A_{p,i}}{A_{m,i}} \quad (25)$$

Table 1

Error Analysis of Figure 12 for Total Attenuation

Frequency 19.701 GHz

		Part 1			Part 2		
		$\mu[\%]$	$\sigma[\%]$	$\rho[\%]$	$\mu[\%]$	$\sigma[\%]$	$\rho[\%]$
2018	WRF	21.01	17.47	27.33	72.59	17.94	74.77
	MultiEXCELL	12.12	9.22	15.22	29.67	19.7	35.61
2019	WRF	21.67	14.62	26.14	56.35	8.9	57.05
	MultiEXCELL	13.49	6.26	14.87	12.96	3.22	13.35
2018–2019	WRF	21.66	15.64	26.72	64.69	13.4	66.06
	MultiEXCELL	13.16	7.89	15.34	20.97	9.9	23.19

Frequency 39.402 GHz

		Part 1			Part 2		
		$\mu[\%]$	$\sigma[\%]$	$\rho[\%]$	$\mu[\%]$	$\sigma[\%]$	$\rho[\%]$
2018	WRF	33.01	8.41	34.07	59.57	9.44	60.32
	MultiEXCELL	4.01	1.74	4.37	21.7	12.62	25.1
2019	WRF	40.23	9.42	41.32	51.2	2.06	51.24
	MultiEXCELL	9.64	5.09	10.9	11.09	6.01	12.62
2018–2019	WRF	36.69	8.57	37.68	54.63	4.93	54.85
	MultiEXCELL	6.95	3.06	7.6	15.2	3.41	15.58

Note. μ , σ , and ρ are mean, standard deviation, and r.m.s of relative error. Measurement curve is considered as the reference value in error analysis. Data for comparison of prediction methods are tabulated at fixed probability levels: Part 1 = [0.1, 0.2, 0.3, 0.5, 1]% and Part 2 = [0.03, 0.05, 0.1]%.

where S_i is the ratio calculated for the i th radio link. The natural logarithm of the ratio is used as a test variable. To compensate the effects of contributions from attenuation sources other than rain as well as from measurement inaccuracies, which predominantly affect the lower attenuation values, a modification should be done. For attenuation less than $A_{m,i} < 10$ dB, the logarithm is multiplied by a scale factor. This scale factor is a power function of the measured attenuation. So the test variable will be

$$V_i = \ln(S_i) \left(\frac{A_{m,i}}{10} \right)^{0.2} \quad \text{for } A_{m,i} < 10 \text{ dB} \\ = \ln(S_i) \quad \text{for } A_{m,i} \geq 10 \text{ dB} \quad (26)$$

Then, calculate the mean μ_V , standard deviation σ_V , and r.m.s value ρ_V for the variable V over each percentage of time:

$$\rho_V = \sqrt{\mu_V^2 + \sigma_V^2} \quad (27)$$

Table 1 presents the error analysis of simulations results with respect to measurements considered as reference values. Since there is a clear difference in behavior between the lowest percentages part and the highest percentages part of the graph, it has been decided to separate the percentages of time into two parts for error calculation. Part 1 corresponds to the time percentages of [0.1, 0.2, 0.3, 0.5, 1]% and Part 2 to [0.03, 0.05, 0.1]%. The lowest percentages of time (0.01% and 0.02%) have been discarded because they correspond to the high attenuation saturation region of the beacon receiver. At 19.7 GHz for Part 1, the r.m.s error for WRF and MultiEXCELL are in the range of 26% and 15% of the year, respectively. This result clearly indicates the good performance of MultiEXCELL for the highest time percentages. In Part 2, the precision of MultiEXCELL reduces, for the 2 years period, the r.m.s error reaches 23%, compared to the WRF r.m.s of 66%. For 39.402 GHz, the performances of MultiEXCELL increase.

7. Conclusion

The new model presented in this paper uses the output data of WRF and combines them with MultiEXCELL model to create synthetic rain events with high spatial resolution. An image processing technique named Optical Flow is used for the detection of the movement of rain cells in the 2D-rain maps coming from WRF. As this technique is appropriate only for gray scale images, the rain rate data is transformed into normalized reflectivity. Using the rain motion flow between two consecutive time samples, the rain rate data maps are estimated every minute, increasing the time resolution to 1 min.

The overall model consists in a combination of WRF, MultiEXCELL, and Optical Flow techniques. It creates an efficient method to generate more realistic rain attenuation time series. Long-term CCDF statistics of attenuation data are validated by comparison with the Alphasat beacon measurements over 2 years at Louvain-la-Neuve ground station.

The model can now been used for generating attenuation time series for non-geostationary Earth-space links and further ACM testing in the design phase of non-geostationary satellites. As soon as attenuation measurements of LEO satellites will be available, the model will be validated for non-geostationary links.

Data Availability Statement

The daily data of Alphasat receiver station can be visualized on the website at <http://130.104.205.199:8080/alphasat/graphs/today.html>. The statistics and simulation data represented in this paper for the period of 1 September 2018 to 30 August 2020 can be accessed publicly at the <https://doi.org/10.5281/zenodo.7422325>.

Acknowledgments

The Université catholique de Louvain is thanked for the access to the Alphasat ground station data.

References

- Ayzel, G., Heistermann, M., & Winterrath, T. (2019). Optical flow models as an open benchmark for radar-based precipitation nowcasting (rainymotion v0.1). *Geoscientific Model Development*, 12(4), 1387–1402. <https://doi.org/10.5194/gmd-12-1387-2019>
- Baker, S., Scharstein, D., Lewis, J. P., Roth, S., Black, M. J., & Szeliski, R. (2011). A database and evaluation methodology for optical flow. *International Journal of Computer Vision*, 92(1), 1–31. <https://doi.org/10.1007/s11263-010-0390-2>
- Barron, J. L., Fleet, D. J., & Beauchemin, S. S. (1994). Performance of optical flow techniques. *IJCV*, 12(1), 43–77. <https://doi.org/10.1007/bf01420984>
- Besnerais, G. L., & Champagnat, F. (2005). Dense optical flow by iterative local window registration. *Proceedings of International Conference on Image Processing, ICIP*, (Vol. 1, pp. 134–137). <https://doi.org/10.1109/ICIP.2005.1529706>
- Bryant, G. H., Adimula, I., Riva, C., & Brussaard, G. (2001). Rain attenuation statistics from rain cell diameters and heights. *International Journal of Satellite Communications*, 19(3), 263–283. <https://doi.org/10.1002/sat.673>
- Capsoni, C., Fedi, F., Magistroni, C., Paraboni, A., & Pawlina, A. (1987). Data and theory for a new model of the horizontal structure of rain cells for propagation applications. *Radio Science*, 22(3), 395–404. <https://doi.org/10.1029/RS022i003p00395>
- Capsoni, C., Luini, L., Paraboni, A., Riva, C., & Martellucci, A. (2009). A new prediction model of rain attenuation that separately accounts for stratiform and convective rain. *IEEE Transactions on Antennas and Propagation*, 57(1), 196–204. <https://doi.org/10.1109/TAP.2008.2009698>
- Castanet, L., Bolea-Alamañac, A., & Bousquet, M. (2003). Interference and fade mitigation techniques for Ka and Q/V band satellite communication systems. In *Proceedings of 2nd International Workshop of Cost Action (Vol. 280)*.
- ESA/ESTEC contract 105326. (2015). *Channel modelling for design of earth observation Ka band data downlink systems (Tech. Rep.)*. ONERA (F), UCL (B), PoLiMi (I), TAS-I (I).
- Fayon, G., Féral, L., Castanet, L., Jeannin, N., & Boulanger, X. (2017). Use of WRF to generate site diversity statistics in south of France. In *2017 XXXII Ind General Assembly and Scientific Symposium of the International Union of Radio Science (URSI GASS)* (pp. 1–4).
- Gallinaro, G., Vernucci, A., & Moreau, C. (2005). Protocols and signalling for fade mitigation techniques (FMT) in DVB-RCS multi-beam systems: Final report.
- Heistermann, M., Jacobi, S., & Pfaff, T. (2013). An open source library for processing weather radar data (wradlib). *Hydrology and Earth System Sciences*, 17(2), 863–871. <https://doi.org/10.5194/hess-17-863-2013>
- Hodges, D. D., Watson, R. J., & Wyman, G. (2006). An attenuation time series model for propagation forecasting. *IEEE Transactions on Antennas and Propagation*, 54(6), 1726–1733. <https://doi.org/10.1109/TAP.2006.875501>
- ITU-Radio Communication Study Groups. (2016). Test variables for the selection of prediction methods (Tech. Rep.). Retrieved from <https://www.itu.int/oth/R0A04000007/en>
- ITU-R P.1853-2 (2019). *Time series synthesis of tropospheric impairments (Tech. Rep.)*. ITU. Retrieved from <http://www.itu.int/ITU-R/go/patents/en>
- ITU-R P.618-13 (2017). *Propagation data and prediction methods required for the design of Earth-space telecommunication systems (Tech. Rep.)*. International Telecommunication Union. Retrieved from <https://www.itu.int/rec/R-REC-P.618/en>
- ITU-R Recommendation P.838-3 (2005). Specific attenuation model for rain for use in prediction methods (Tech. Rep.). Retrieved from <https://www.itu.int/rec/R-REC-P.838-3-200503-I/en>
- ITU-R Recommendation P.840-7 (2017). *Attenuation due to clouds and fog (Tech. Rep.)*. International Telecommunication Union. Retrieved from <https://www.itu.int/rec/R-REC-P.840/en>
- Jeannin, N., Castanet, L., Dahman, I., Pourret, V., & Pouponneau, B. (2019). Smart gateways switching control algorithms based on tropospheric propagation forecasts. *International Journal of Satellite Communications and Networking*, 37, 43–55. <https://doi.org/10.1002/sat.1233>

- Jeannin, N., & Dahman, I. (2016). Sizing and optimization of high throughput radio-frequency data down link of Earth observation satellites. *International Journal of Satellite Communications and Networking*, 34(2), 231–250. <https://doi.org/10.1002/sat.1115>
- Jeannin, N., Dahman, I., Castanet, L., Pourret, V., & Pouponneau, B. (2016). Tropospheric propagation forecasts for smart gateways switching algorithms. In *2016 8th Advanced Satellite Multimedia Systems Conference and the 14th Signal Processing For Space Communications Workshop* (pp. 1–8). ASMS/SPSC.
- Jeannin, N., Outeiral, M., Castanet, L., Pereira, C., Vanhoenacker-Janvier, D., Riva, C., et al. (2014). Atmospheric channel simulator for the simulation of propagation impairments for Ka band data downlink. In *8th European Conference on Antennas and Propagation, EuCAP 2014* (pp. 3357–3361). <https://doi.org/10.1109/EuCAP.2014.6902547>
- Luini, L., & Capsoni, C. (2011). MultiEXCELL: A new rain field model for propagation applications. *IEEE Transactions on Antennas and Propagation*, 59(11), 4286–4300. <https://doi.org/10.1109/TAP.2011.2164175>
- Marziani, A., Consalvi, F., Fusco, G., Riva, C., Luini, L., & Parodi, A. (2019). Microwave tropospheric scintillation and excess attenuation prediction for satellite to Earth links using 3d high-resolution meteorological forecast models: Data validation and case study. In *2019 Photonics & Electromagnetics Research Symposium* (pp. 3405–3411). PIERS-Spring.
- NCAR. (2022). User's guides for the advanced research WRF (ARW) modeling system (Tech. Rep.). Retrieved from https://www2.mmm.ucar.edu/wrf/users/docs/user_guide_v4/contents.html
- NOAA. (2022). Earth System Research Laboratory. Retrieved from https://esrl.noaa.gov/gsd/wrfportal/namelist_input_options.html
- Outeiral García, M., Jeannin, N., Féral, L., & Castanet, L. (2013). Use of WRF model to characterize propagation effects in the troposphere. In *7th European Conference on Antennas and Propagation (EuCAP)*. IEEE.
- Pereira, C., Vanhoenacker-Janvier, D., Jeannin, N., Castanet, L., & Martellucci, A. (2014). Simulation of tropospheric scintillation on LEO satellite link based on space-time channel modeling. In *8th European Conference on Antennas and Propagation, EuCAP 2014*. <https://doi.org/10.1109/EuCAP.2014.6902588>
- Quibus, L. (2020). *Modelling propagation impairments of Earth-Space links using Numerical Weather Prediction tools (PhD thesis)*. Université catholique de Louvain.
- Quibus, L., Luini, L., Riva, C., & Vanhoenacker-Janvier, D. (2019). Use and accuracy of Numerical Weather Predictions to support EM wave propagation experiments. *IEEE Transactions on Antennas and Propagation*, 67(8), 5544–5554. <https://doi.org/10.1109/tap.2019.2913785>
- Recommendation ITU-R P.1623-1. (2003). Prediction method of fade dynamics on Earth-space paths (Tech. Rep.) (pp. 1623–1631). Retrieved from <https://www.itu.int/rec/R-REC-P.1623/en>
- Sánchez Pérez, J., Meinhart-Llopis, E., & Facciolo, G. (2013). TV-L1 optical flow estimation. *Image Processing On Line*, 3, 137–150. <https://doi.org/10.5201/ipol.2013.26>
- Skamarock, W. C., Klemp, J. B., Dudhia, J., Gill, D. O., Liu, Z., Berner, J., et al. (2021). *A description of the advanced research WRF model Version 4.3* (Tech. Rep.). NCAR/UCAR.